coatings

MDPI

Article

Numerical Simulation and Mechanism of Line Uniformity for Aerosol Jet-Printed Diamond Coatings

Hao Chang [1], Qingyu Yao [2,*], Xiaofei Xie [2] and Mohammad Uddin [3]

[1] College of Intelligent Manufacturing, Zhengzhou Technical College, Zhengzhou 450121, China; changhaosc@163.com
[2] Faculty of Engineering, Huanghe Science and Technology University, Zhengzhou 450003, China
[3] School of Electrical and Mechanical Engineering, Adelaide University, Adelaide, SA 5005, Australia; mohammad.uddin@adelaide.edu.au
* Correspondence: qingyu.yao@hhstu.edu.cn

Highlights

- This paper revealed the dynamic evolution laws of droplet deposition under low-speed and high-speed jetting in aerosol jet printing (AJP) and clarified the morphological evolution characteristics and final forming differences in droplets in the thickness and diameter directions under different jetting speeds.
- A transient numerical model for AJP droplet deposition based on computational fluid dynamics (CFD) was constructed. The volume of fluid (VOF) and discrete phase model (DPM) methods were coupled to accurately capture the liquid–gas interface and the movement of diamond particles. The simulation accuracy is high, with an error control within ±10%. It is highly consistent with the experimental results, and the model has strong reliability.
- For the AJP preparation process of diamond coatings on micro-milling cutters with a large aspect ratio, the key process parameters for droplet deposition were quantitatively determined. The value of the adjacent printing line spacing that can achieve continuous lines without gaps under the key process parameters was obtained, providing direct data support for the control of coating uniformity.

Abstract

The large aspect ratio micro end mill is a critical tool for microstructure machining, and its performance directly determines processing quality and efficiency. Diamond coatings are commonly applied to cutting edges to enhance wear resistance and extend tool life. However, existing coating techniques often suffer from poor uniformity and inadequate consistency, limiting batch production and process stability. Aerosol jet printing (AJP) offers a cost-effective and highly controllable alternative for the efficient, large-scale deposition of diamond coatings on micro end mills, where precise control of line spacing is essential to achieving coating uniformity. In this study, a transient numerical model of droplet deposition in AJP is developed using computational fluid dynamics (CFD). The volume of fluid (VOF) method and the discrete phase model (DPM) are coupled to track liquid–gas interface deformation and diamond particle motion, enabling the dynamic evolution of droplet deposition to be captured. The effects of inter-droplet distance on deposition, spreading, coalescence, and line uniformity are systematically investigated. Droplet deposition mechanisms are analyzed under low-speed jetting conditions, while high-speed jetting simulations are conducted to reflect industrial processing scenarios. The results show that under low-speed jetting, droplets undergo spreading, contraction, and rebound, eventually forming a uniform cap-like structure. Under high-speed jetting, droplets exhibit

Check for updates

Academic Editor: Bohayra Mortazavi

Received: 16 July 2026
Revised: 6 August 2026
Accepted: 7 August 2026
Published: 10 August 2026

Copyright: © 2026 by the authors. Licensee MDPI, Basel, Switzerland. This article is an open access article distributed under the terms and conditions of the Creative Commons Attribution (CC BY) license.

a dispersed ring-shaped spreading pattern; although uniformity is slightly reduced, the spreading area and deposition efficiency are significantly increased. These findings provide a theoretical basis for optimizing AJP process parameters to achieve high-quality diamond coatings on micro end mills.

Keywords: aerosol jet printing; numerical simulation; droplet deposition mechanism; line uniformity

1. Introduction

The large aspect ratio micro-milling cutter is a fundamental tool for microstructure machining. Its service performance directly dictates both the quality and efficiency of the process. Current milling cutters use cemented carbide as the substrate material, for which a diamond coating is required to enhance wear resistance and extend tool service life [1,2]. However, conventional techniques such as chemical vapor deposition (CVD) and physical vapor deposition (PVD) often suffer from limited coating uniformity and inadequate interfacial adhesion between the coating and the substrate [3]. Aerosol jet printing offers distinct advantages for this application, including micrometer-scale forming accuracy and precise selective deposition [4–6]. These capabilities position it as a promising technology for depositing diamond coatings on large aspect ratio micro-milling cutters [7–9]. During printing, the uniformity of the deposited lines governs the flatness and adhesion strength of the resulting diamond coating [10]. Improper selection of line gap parameters can lead to coating overlap or uneven spacing, compromising the protective performance of the coating and increasing the risk of edge chipping. This underscores the need for a fundamental understanding of the underlying processing mechanisms [11].

In recent years, numerical simulations have been conducted on the processing mechanisms of aerosol jet printing, providing a theoretical foundation for the precision deposition of diamond coatings. Jin et al. [12] developed a complete AJP model based on CFD to predict the jetting and deposition processes. The gas and liquid flows are described using the VOF model; the movement of aerosol particles is captured through the DPM; and the film formed by particle deposition is monitored using the eulerian wall films (EWF) model. The EWF-VOF structure enables the conversion between the liquid film and the fluid phase. The DPM-VOF model converts the particles impacting the deposit into the corresponding fluid phase volume. Liu et al. [13] developed a three-dimensional numerical model that couples CFD with the DPM framework. The model, which integrates the Taylor analogy breakup model, was used to evaluate droplet flow behavior after nozzle ejection, with particular focus on the regulatory effect of Saffman lift. Experimental validation confirmed that the model predictions closely matched the measured printing line widths, providing a robust quantitative basis for parameter optimization. To address dimensional accuracy challenges in drop-on-demand inkjet printing, Elkaseer et al. [14] developed a geometry-based simulation tool. The model incorporated key factors affecting print quality, including droplet volume, contact angle, and droplet fusion behavior. By simulating droplet spreading and stacking on the substrate, the study elucidated how image resolution and droplet diameter govern the dimensional accuracy of printed features, offering valuable guidance for numerical simulations in inkjet printing. Shah et al. [15] developed a computational model using the VOF method. By solving the Navier–Stokes and continuity equations, the model accurately captured droplet impact, spreading, and rebound dynamics on solid surfaces. The simulations revealed how surface tension and contact angle influence printing quality, providing key theoretical insights for analyzing diamond droplet deposition on cemented carbide substrates.

While progress has been made in numerical simulations of line formation and deposition mechanisms in aerosol jet printing, quantitative studies on printed line uniformity and the development of corresponding simulation models remain limited. This study addresses the requirements for diamond coating deposition on high-aspect-ratio micro-milling cutters made of cemented carbide. A transient simulation model of droplet behavior during aerosol jet printing was developed. The model focuses on the underlying mechanisms of droplet deposition and line formation, revealing how key process parameters influence line uniformity. Based on these insights, the process parameters were optimized to achieve uniform diamond coatings on high-aspect-ratio micro-milling cutters, providing theoretical and technical guidance for enhancing cutter performance.

2. Numerical Methods

The ink is atomized by an aerosol generator into a cloud of micron-sized droplets. Entrained by a carrier gas, the droplet stream is then directed through a micro-nozzle and propelled along a predefined trajectory before being precisely deposited onto the substrate surface. Upon impact with the substrate, the droplets rapidly spread to form a liquid film, driven by the interplay of inertial forces, surface tension, and viscosity. Simultaneously, the nozzle continues its programmed trajectory to complete the area printing [16]. Schematic diagram of the aerosol jet printing process, as shown in Figure 1. The inter-line gap is a critical parameter governing printing uniformity. An excessive gap leads to incomplete coverage (gaps between lines), whereas an insufficient gap results in localized overlapping.

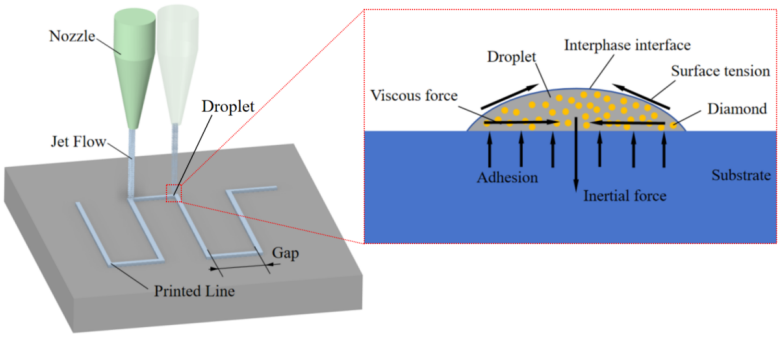


Figure 1. Schematic of the aerosol jet printing process.

To reveal the deposition mechanism of droplets impacting, spreading, and forming a liquid film on the substrate, a theoretical analysis was conducted and a simulation model conforming to actual working conditions was established. As this process involves multiphase flow, accurate tracking of the droplet interface is essential for describing droplet dynamics. Using the VOF method to track the transient deformation of the droplet interface effectively addresses the aforementioned challenges. The diamond particles contained within the droplets were tracked using the DPM. The forces acting on the droplet upon impact with the substrate are illustrated in Figure 1. Upon droplet impact, four primary forces govern its behavior. Surface tension, arising from molecular interactions at the droplet interface, acts tangentially and drives droplet retraction. Concurrently, inertial force promotes radial spreading upon impact. Adhesion force, resulting from interactions between the diamond particles, solvent, and substrate atoms, acts upward normal to the substrate. Viscous force, originating from the ink's high viscosity, resists droplet flow and deformation [17].

2.1. Control Equation

In the VOF method, the liquid–gas interface is tracked by solving the phase volume fraction equation, governed by [18,19]:

$$\frac{\partial \alpha}{\partial t} + \vec{u} \cdot \nabla \alpha = \mathbf{0} \tag{1}$$

In the equation, α represents the volume fraction of the liquid phase ($\alpha = 1$ indicates the liquid phase, $\alpha = 0$ indicates the gas phase, and $0 < \alpha < 1$ represents the liquid–gas interface region); t is the time (s); $\vec{u}$ is the velocity vector of the liquid phase (m/s).

The Navier–Stokes equations describe the behavior of incompressible fluids and elucidate the dynamic process of droplet impacting a surface. Among them, the continuity equation is expressed as [20–22]:

$$\frac{\partial \rho}{\partial t} + \nabla \cdot \left(\rho \vec{u}\right) = \mathbf{0} \tag{2}$$

where ρ is the density (kg/m^3).

The momentum equation can be expressed as [23,24]:

$$\frac{\partial \left(\rho \vec{u}\right)}{\partial t} + \nabla \cdot \left(\rho \vec{u} \vec{u}\right) = -\nabla p + \nabla \cdot \left[\mu \left(\nabla \vec{u} + \nabla \vec{u}^{T}\right)\right] + \rho \vec{g} + \overrightarrow{F_{\gamma}} + \overrightarrow{F_{ad}} \tag{3}$$

where p is the pressure (Pa); μ is the dynamic viscosity (Pa·s); $\vec{g}$ is the gravitational acceleration (m/s^2); $\vec{F_{\gamma}}$ is the surface tension, which can be calculated through $\vec{F_{\gamma}} = \gamma \rho \kappa \nabla \alpha$, the surface tension coefficient; κ is interface curvature; $\vec{F_{ad}}$ is the adhesion, which can be calculated through $\vec{F_{ad}} = k_{ad} \cdot \frac{\alpha}{h} \cdot \vec{n}$; k_{ad} is the adhesion coefficient; h is the thickness of the liquid–solid contact layer; $\vec{n}$ is the surface normal vector.

The motion of diamond particles within the droplet was tracked using the DPM, considering the effects of drag, gravity, pressure gradient, and virtual mass forces. The equation governing particle motion is given by [25–29]:

$$m_p \frac{d\overrightarrow{u_p}}{dt} = \overrightarrow{F_D} + \overrightarrow{F_G} + \overrightarrow{F_P} + \overrightarrow{F_{VM}} \tag{4}$$

where the expressions for gravity ($\vec{F_G}$), the pressure gradient force ($\vec{F_P}$), and the virtual mass force ($\vec{F_{VM}}$) are as follows:

$$\begin{aligned} \vec{F}_G &= m_p \vec{g} \left(\mathbf{1} - \frac{\rho}{\rho_p}\right) \\ \vec{F}_p &= V_p \nabla p = \frac{\pi d_p^{\,3}}{\mathbf{6}} \nabla p \\ \vec{F}_{VM} &= C_{VM} \rho V_p \left(\frac{d\vec{u}}{dt} - \frac{d\overrightarrow{u_p}}{dt}\right) \end{aligned} \tag{5}$$

In the equation, ρ_p is the density of diamond particles (kg/m^3); C_{VM} is the virtual mass force coefficient (the spherical particles are set at 0.5).

The expression for the viscous drag force ($\vec{F_D}$) of the liquid on the particles:

$$\vec{F_D} = \frac{\mathbf{1}}{\mathbf{2}} C_D \rho \frac{A_p}{m_p} \left|\vec{u} - \vec{u_p}\right| \left(\vec{u} - \overrightarrow{u_p}\right) \tag{6}$$

where the C_D is the drag coefficient, $A_p = \pi d_p^{\,2}/4$ is the projected area of the particle, d_p is the particle diameter, and $\vec{u_p}$ is the particle velocity vector.

2.2. Simulation Model

The droplet deposition model was established for two parallel droplets on adjacent lines. The following assumptions were made in the simulations:

(1) Based on the conservation of mechanical energy ($mgh = \frac{m(v^2 - v_0^2)}{2}$, v_0 represents the initial velocity of the droplet position, v represents the speed at which the droplet reaches the surface of the substrate), the change in droplet velocity due to the working distance h is negligible and can be ignored in the simulations;
(2) Given that individual differences among droplets are negligible after uniform atomization, the droplet stream ejected from the nozzle can be treated as a single aggregated cluster;
(3) To eliminate the effects of surface roughness on droplet dynamics, the substrate was modeled as an ideally smooth surface. Additionally, the influence of substrate temperature during printing was neglected.

A droplet deposition simulation model was established, with a cylindrical domain measuring 55 μm in height and 240 μm in diameter. The model was discretized using a hexahedral mesh. A mesh independence test balancing accuracy and efficiency was performed using three hexahedral mesh sizes (2 μm, 1 μm and 0.5 μm). Droplet maximum spreading diameter, equilibrium diameter and stabilization time were compared. All key parameters differed by less than 3% between the 1 μm and 0.5 μm meshes; finer grids offered negligible accuracy gains but greatly increased computation time. Thus, the 1 μm mesh (2,499,860 elements) was chosen, with full comparison data listed in Table 1. A pressure-based solver was used for the simulations, with gravity enabled. A no-slip wall condition was imposed at the bottom boundary [15], as illustrated in Figure 2a.

Table 1. The mesh independence test.

Mesh Size	Total Elements	Max Spreading Diameter	Equilibrium Diameter	Stabilization Time
2 μm	624,972	49.5 μm	32.0 μm	91.8 μs
1 μm	2,499,860	51.2 μm	33.1 μm	87.2 μs
0.5 μm	9,987,541	51.7 μm	33.5 μm	86.5 μs

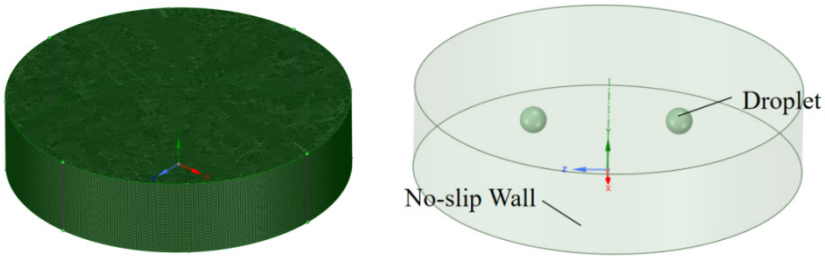


Figure 2. Schematic diagram of simulation. (**a**) Computational domain and grid division; (**b**) simulation model and boundaries.

To investigate droplet behavior on adjacent printing lines, a simulation model incorporating two adjacent droplets was established. The two droplets deposit sequentially rather than simultaneously, with the process comprising two stages: deposition of the first droplet, followed by deposition of the second droplet. First, the first droplet was deposited on the substrate and allowed to reach a stable equilibrium. Subsequently, the second droplet was deposited, and the simulation was continued until the system again attained a steady state. To investigate the effect of line spacing on printing uniformity, the distance between two droplets was used to represent the spacing of adjacent printed lines. Simulations of droplet deposition were then performed for various inter-droplet distances.

The droplet region was selected using the cell register, and its initial position was defined during global initialization via the Patch method. The droplets were set to a

diameter of 20 μm with an initial height of 30 μm above the substrate. The numerical simulations were implemented with ANSYS Fluent 2023. The bottom surface of the model adopts the no-slip wall boundary condition, while the sides and the top surface adopt the pressure outlet boundary condition, as illustrated in Figure 2b. The number of diamond particles within the droplet is calculated based on the density and volume of the diamond particles and the ink. For a 20 μm droplet, the number of encapsulated diamond particles was estimated to be 3300. The transient simulations were conducted using the Pressure-Velocity Coupling and Pressure-Implicit with Splitting of Operators (PISO) scheme. Least Squares Cell-Based is selected as the gradient reconstruction method, and Second Order Upwind is used for the discretization of the momentum equation, with a time step of 0.02 μs to ensure numerical stability and accuracy.

2.3. Material Parameter

The droplet ink was formulated by mixing deionized water, 95% ethanol, and diamond particles (60,000 mesh). The average size of the diamond particles was determined to be 0.25 μm. The contact angle and viscosity of the ink were measured using a SR-180S contact angle tester manufactured by Shuorui Technology (Jiangmen, China) and a LD-WND viscosity measuring instrument from Shandong Lanende Intelligent Technology (Weifang, China), respectively; the physical properties of both the ink and air are provided in Table 2.

Table 2. Physical property parameters.

Material	Density	Viscosity	Contact Angle	Surface Tension Coefficient
Ink	1140 kg/m^3	4.7×10^{-3} kg/(m·s)	61.2°	44 mN/m
Air	1.225 kg/m^3	1.8×10^{-5} kg/(m·s)		

3. Low-Speed Jet Printing Results and Discussion

At low speeds, the droplets undergo a complete dynamic evolution process from flight, collision with the substrate, to final stabilization, which helps to clearly reveal the mechanism of droplet deposition and morphological evolution. Although the low-speed process has significant research value, due to the limitations of experimental observation methods, when the jetting speed is too low, it is impossible to directly capture the complete dynamic process of droplets from falling to deposition. Moreover, under this low-speed condition, the printing effect is weak and has no practical observation or application value. Therefore, this study uses an aerosol jet printing device to conduct numerical simulations under the critical minimum speed condition for droplet discharge, in order to make up for the deficiencies of experimental observation and conduct detailed observation and mechanism analysis of this low-speed process. The simulation selects a main airflow flow rate of 10 mL/min and a nozzle diameter of 100 μm. The initial droplet speed is determined to be 21.22 m/s through the flow velocity calculation formula, and the droplet spacing is set to 50 μm. The movement and diffusion behavior of the droplets are systematically studied. The research results can provide theoretical support for the mechanism analysis and parameter optimization of the high-speed jetting process, as well as the future development of precision printing technology based on low-speed aerosol jetting.

3.1. Simulation Results at 50 μm Droplet Spacing

The dynamic spreading and morphological evolution of the first droplet upon impacting the cemented substrate can be divided into three stages: initial contact, rapid spreading, and contraction to equilibrium, as shown in Figure 3. The initial contact stage occurs from 0 to 1.0 μs. Upon impact at t = 0 μs, the droplet is approaching the substrate in a

spherical shape but has not yet made contact. By t = 1.0 μs, its bottom has fully wetted the substrate, characterized by a decrease in height and an onset of lateral spreading. This stage is governed primarily by the coupled effects of inertial and adhesion forces. Inertia drives the droplet toward the substrate, while adhesion overcomes surface tension, promoting rapid wetting. Owing to the extremely short timescale, viscous forces remain negligible and do not significantly impede flow. The rapid spreading stage occurs from 1.0 to 3.0 μs. During this period, the droplet continues to expand laterally, evolving into a disk-like shape with a progressively thinning liquid film. Inertial force remains the dominant driver of spreading. However, due to the presence of diamond particles, the ink exhibits increased viscosity, and the resulting viscous force begins to impede further expansion. Consequently, the spreading rate gradually decreases over time, although lateral growth persists. The stabilization stage occurs from 3.0 to 100.0 μs. Following maximum spreading, the droplet begins to retract and gradually stabilize. As the droplet recedes to a critical extent, surface tension becomes dominant and, together with viscous forces, counteracts the remaining inertia, driving the droplet toward equilibrium. The resulting steady-state droplet dimension directly defines the single-line feature size in aerosol jet printing, serving as the fundamental building block for subsequent line overlap and coating formation.

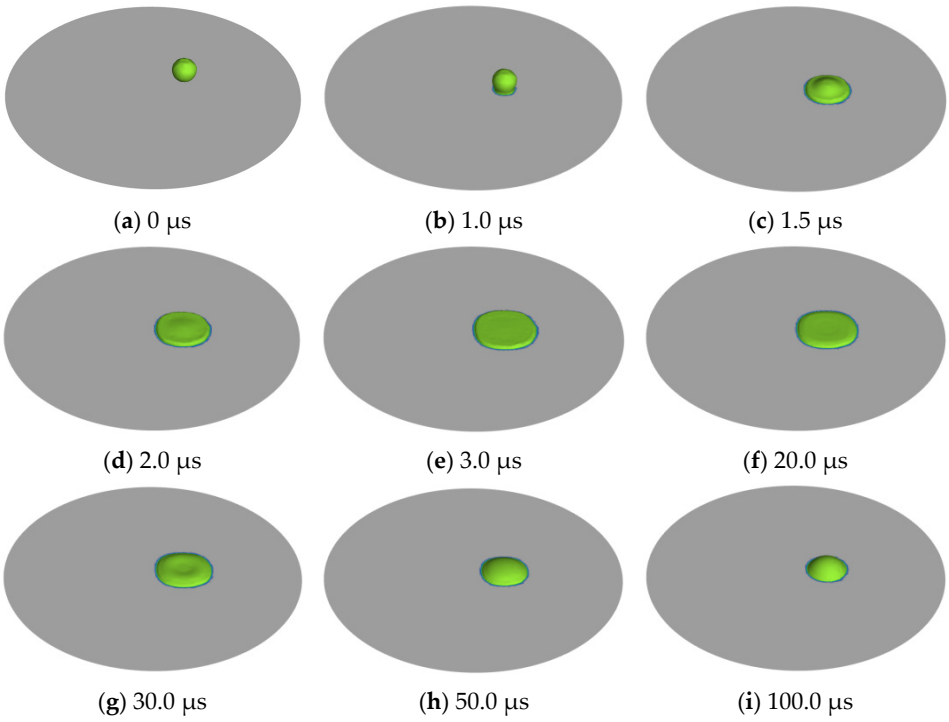


Figure 3. The movement process of the first droplet. (**a**) 0 μs; (**b**) 1.0 μs; (**c**) 1.5 μs; (**d**) 2.0 μs; (**e**) 3.0 μs; (**f**) 20.0 μs; (**g**) 30.0 μs; (**h**) 50.0 μs; (**i**) 100.0 μs.

Figure 4 illustrates the impact and deposition behavior of two adjacent droplets during aerosol jet printing. Due to the large separation distance, the droplets do not coalesce upon impacting the substrate. Instead, the second droplet undergoes a deposition process similar to that of the first, exhibiting the same three stages: initial contact, rapid spreading, and contraction to equilibrium. Each droplet thus behaves as an isolated entity, following the diffusion and rebound dynamics characteristic of a single droplet. However, the high viscosity of the ink significantly modulates this behavior, suppressing both diffusion and rebound, thereby highlighting the critical role of viscous effects in droplet dynamics.

The evolution of droplet diameter and height during spreading was quantified by statistical analysis at each time step. The measured dimensions are defined schematically

in Figure 5. Since droplet–substrate contact initiates at t = 1 μs, the statistical analysis was performed from this time onward.

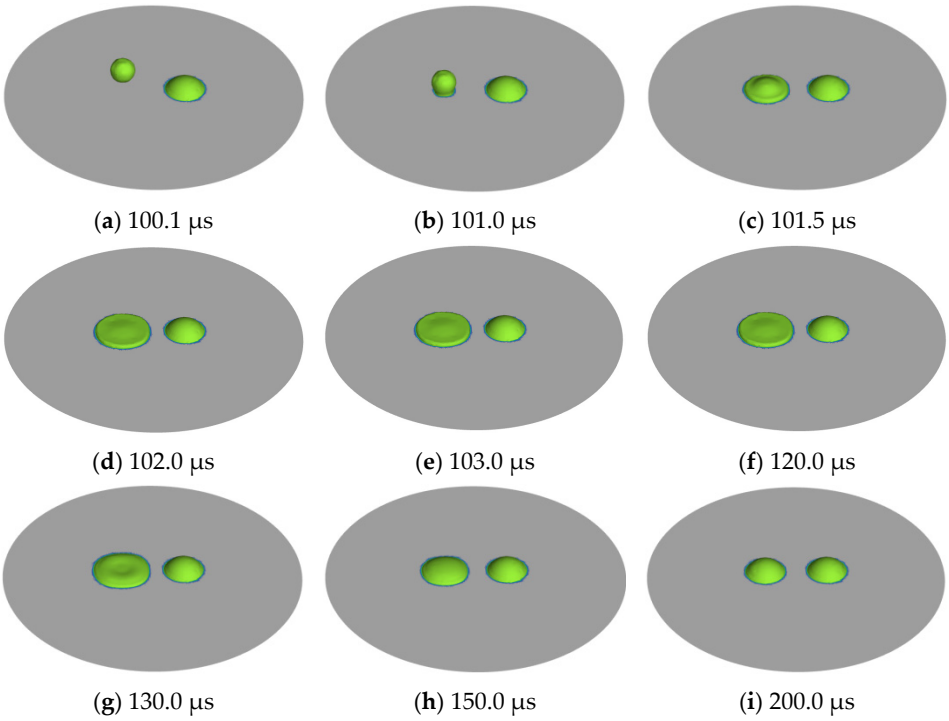


Figure 4. The movement process of the second droplet. (**a**) 100.1 μs; (**b**) 101.0 μs; (**c**) 101.5 μs; (**d**) 102.0 μs; (**e**) 103.0 μs; (**f**) 120.0 μs; (**g**) 130.0 μs; (**h**) 150.0 μs; (**i**) 200.0 μs.

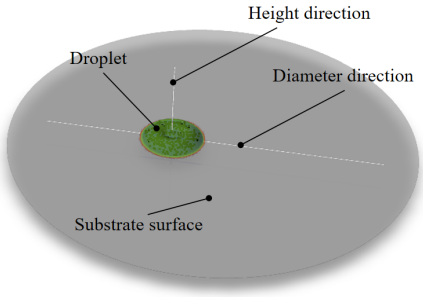
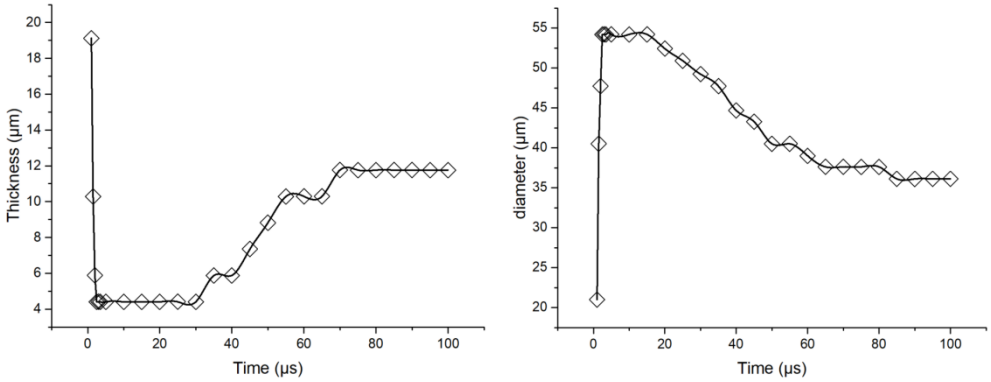


Figure 5. Diagram of droplet statistical analysis.

Figure 6a shows the evolution of droplet thickness upon substrate impact. The thickness profile exhibits three distinct phases: a rapid decay period, a brief stabilization period, and a slow rebound period. The rapid decay phase occurs from 0 to 2.5 μs. This dramatic compression is driven by inertial forces generated during impact, which propel the droplet to spread radially outward. Concurrently, adhesion forces overcome surface tension, facilitating the rapid deformation of the droplet from a spherical to a flattened shape and resulting in the observed sharp decline in thickness. The period from 2.5 to 30 μs corresponds to a transient stable stage. As the droplet approaches its critical spreading diameter, the inertial driving force gradually decays, while surface tension-driven contraction becomes increasingly prominent. This contractile effect, in conjunction with viscous resistance, dissipates the remaining kinetic energy of spreading. Simultaneously, the adhesion force at the droplet–substrate interface saturates as the contact area stabilizes, ceasing to provide further driving force for expansion. During this stage, the morphological evolution of the droplet is governed by the interplay of surface tension, viscous forces, and adhesion. Consequently, the droplet thickness stabilizes temporarily at approximately 4.4 μm, with

only minor adjustments at the edge while the central region remains essentially unchanged. The slow rebound phase occurs from 30 to 70 μs. During this period, the droplet height gradually increases from 4.4 μm to 11.8 μm. This rebound is driven by surface tension-driven contraction, opposed by viscous forces, as the droplet evolves toward its equilibrium shape. The system then reaches a fully stabilized state from 70 to 100 μs, with the droplet height remaining constant at 11.8 μm.



(**a**) (**b**)

Figure 6. Statistical analysis of droplet size variations. (**a**) Thickness direction; (**b**) Diameter direction.

Figure 6b illustrates the dynamic evolution pattern of the droplet diameter after it impacts the substrate surface. Through analysis, it was found that the change in droplet diameter went through a rapid expansion phase and a slow convergence phase. The 0–2.5 μs time period was the rapid expansion phase, during which the diameter increased sharply from approximately 21.0 μm to 51.2 μm, with an increase of 158.1%. The inertial force and adhesion force of the droplet dominated the spreading process, causing the droplet to rapidly spread in all directions, and the diameter increased significantly as the spreading area expanded. The 2.5–100 μs time period was the slow convergence phase, during which the diameter slowly converged from 51.2 μm and finally stabilized at 33.1 μm. The reason for this was the action of surface tension and droplet viscosity, which prevented the spreading area from continuing to expand and eventually converged to a stable value.

3.2. Verification of the Simulation Model

The validity of the simulation model was assessed by comparing the combined result obtained through experimentation and theory with the simulation results. Upon reaching equilibrium, the droplet assumes a spherical cap morphology. The equilibrium diameter of this spherical cap, d_{eqm}, can be expressed as a function of the initial droplet diameter d_0 and the equilibrium contact angle θ_{eqm} [14,30–32], as given in Equation (7).

$$d_{eqm} = d_0 \cdot \sqrt[3]{\frac{8}{\tan\frac{\theta_{eqm}}{2} \cdot \left(3 + \tan^2\frac{\theta_{eqm}}{2}\right)}} \tag{7}$$

Using the simulation parameters, the theoretical equilibrium diameter was calculated to be 31.849 μm. This value deviates from the simulated equilibrium diameter of 33.1 μm by 1.251 μm, corresponding to a relative error of +3.9%. Since this error falls within the acceptable range of ±10%, the simulation model is considered capable of accurately predicting droplet dynamics, thereby validating its reliability [33].

Analysis of the simulation results yielded key parameters for droplet even deposition. Upon impacting the substrate, the droplet attained a maximum spreading diameter of 51.2 μm before stabilizing at an equilibrium diameter of 33.1 μm. Figure 7 illustrates the

contrasting morphologies of two droplets: droplet 1 in its stable equilibrium state and droplet 2 at the moment of maximum spread. The characteristic dimension d directly governs the spacing between adjacent printed lines. Droplet coalescence occurs only when the inter-droplet distance is less than or equal to zero, i.e., when d is non-positive. This implies that setting the printing line gap to the sum of the maximum spreading radius (25.6 μm) and the equilibrium radius (16.55 μm)—yielding a critical value of 42.15 μm—ensures theoretically continuous, gapless film formation.

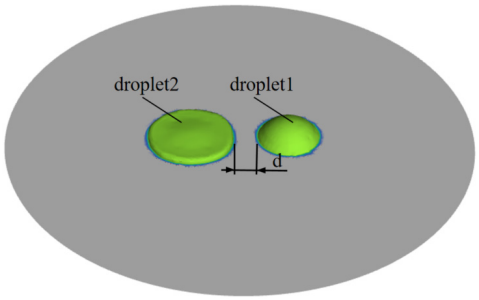


Figure 7. Diagram of droplet spacing.

3.3. Analysis of Droplet Polymerization Process

3.3.1. Simulation Results at 42.15 μm Droplet Spacing

Figure 8 depicts the dynamic evolution of two droplets upon substrate impact at a spacing of 42.15 μm—the critical value identified in this study. Upon impact, inertial forces drive rapid spreading of both droplets. As they approach their maximum diameter, their peripheries meet at the boundary of the adjacent equilibrium droplets. Liquid–gas interfacial interaction induces partial fusion of the contacting regions, forming a transient liquid bridge. As inertial forces dissipate, surface tension-driven contraction becomes dominant, causing the fusion region to gradually recede. Eventually, under the combined influence of surface tension, adhesion, and viscous forces, the system reaches a steady state in which the two droplets separate into distinct, independent forms.

This spacing lies at the critical threshold between line coalescence and inter-line gap formation. While it maintains line continuity, the resulting uniformity is poor, indicating that further optimization of the spacing parameter is necessary to achieve stable droplet fusion and uniform line formation.

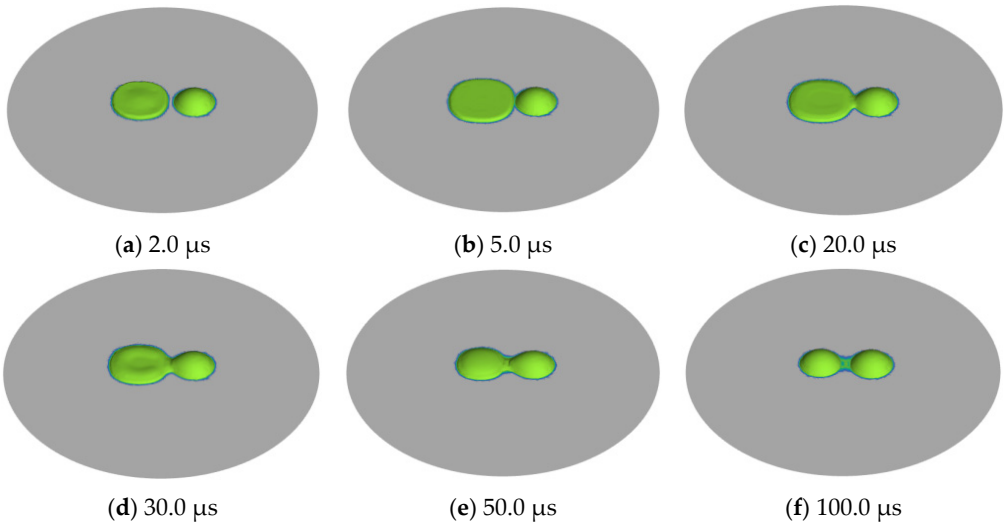
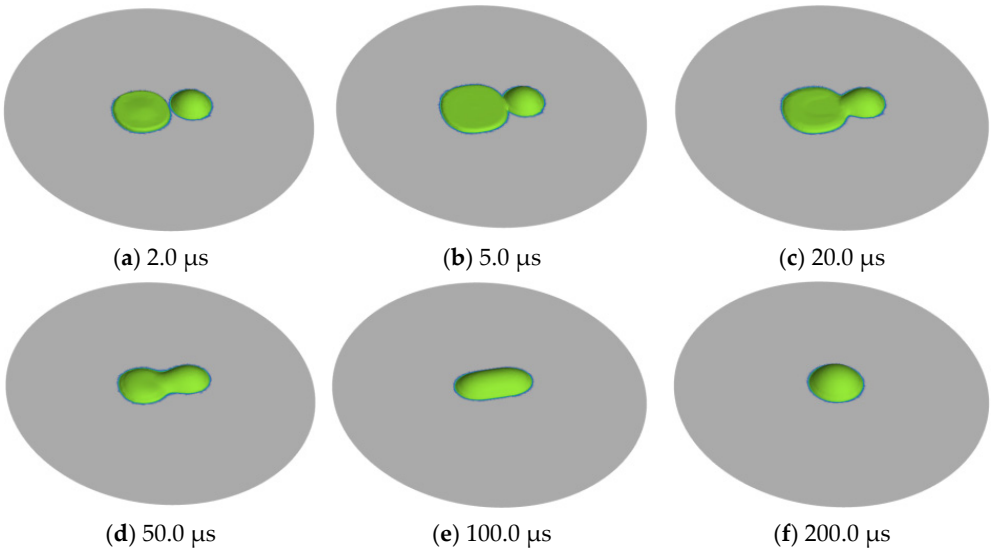


Figure 8. Droplet interaction during impact at a spacing of 42.15 μm. (**a**) 2.0 μs; (**b**) 5.0 μs; (**c**) 20.0 μs; (**d**) 30.0 μs; (**e**) 50.0 μs; (**f**) 100.0 μs.

3.3.2. Simulation Results at 40 μm Droplet Spacing

At a droplet spacing of 40 μm, the following interaction sequence is observed, as shown in Figure 9. Upon impact, inertial forces drive rapid spreading of both droplets, causing their edges to quickly come into contact. Subsequently, liquid–gas interfacial interaction induces partial fusion of the contacting regions, forming a transient liquid bridge. This fusion zone expands progressively over time, eventually leading to complete coalescence of the two droplets into a single continuous liquid film. In the later stage, under the balanced action of surface tension, adhesion, and viscous forces, the coalesced film contracts into a more compact form.



(**a**) 2.0 μs (**b**) 5.0 μs (**c**) 20.0 μs

(**d**) 50.0 μs (**e**) 100.0 μs (**f**) 200.0 μs

Figure 9. Droplet interaction during impact at a spacing of 40 μm. (**a**) 2.0 μs; (**b**) 5.0 μs; (**c**) 20.0 μs; (**d**) 50.0 μs; (**e**) 100.0 μs; (**f**) 200.0 μs.

This behavior demonstrates that a droplet spacing of 40 μm provides sufficient interfacial interaction to overcome localized surface tension-driven contraction, resulting in a continuous deposition unit and achieving the gap-free line formation desired in aerosol jet printing.

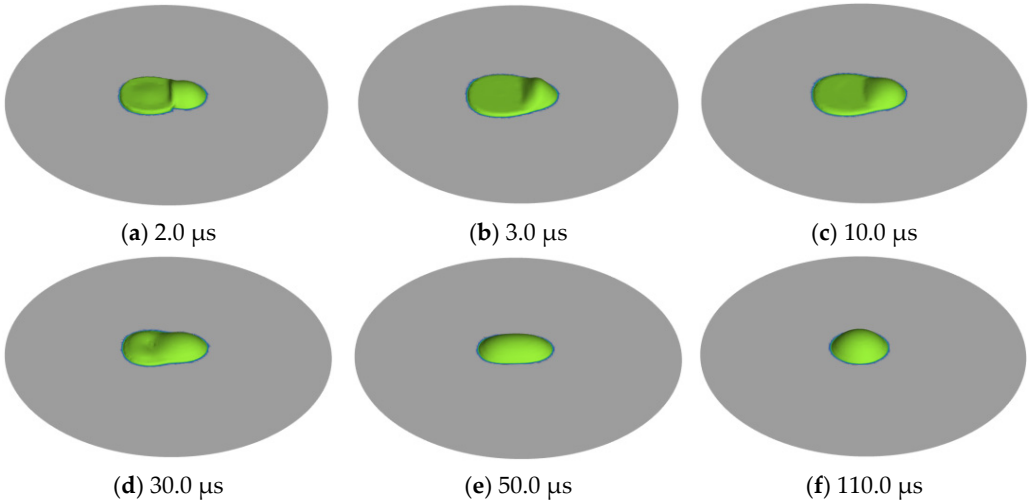
3.3.3. Simulation Results at 36 μm Droplet Spacing

At a droplet spacing of 36 μm, the interaction dynamics differ markedly from the previous cases, as shown in Figure 10. Upon impact, the droplets immediately contact the adjacent steady-state droplets, rapidly forming a locally connected pattern. Subsequently, surface tension-driven contraction promotes swift and complete coalescence into a single continuous liquid film. In the later stage, under the dominance of surface tension, the merged film continues to contract, evolving from a flattened, elongated shape into a stable hemispherical cap.

This behavior indicates that at 36 μm spacing, the droplets undergo immediate aggregation without an independent spreading phase. Compared to the 40 μm case, the stabilization period is shorter and the coalescence efficiency is higher.

To further elucidate the internal flow dynamics, the velocity vector distribution within the droplets was analyzed, as shown in Figure 11. At t = 2 μs, the later-falling droplet exhibits radial outflow from its center, indicating active expansion, with a maximum velocity of 12 m/s. By t = 3 μs, the directional flow is induced from the later-falling droplet toward its earlier-deposited counterpart. The velocity is maximized at the contacting edge interface between the two droplets. At t = 10 μs, the overall flow velocity has diminished

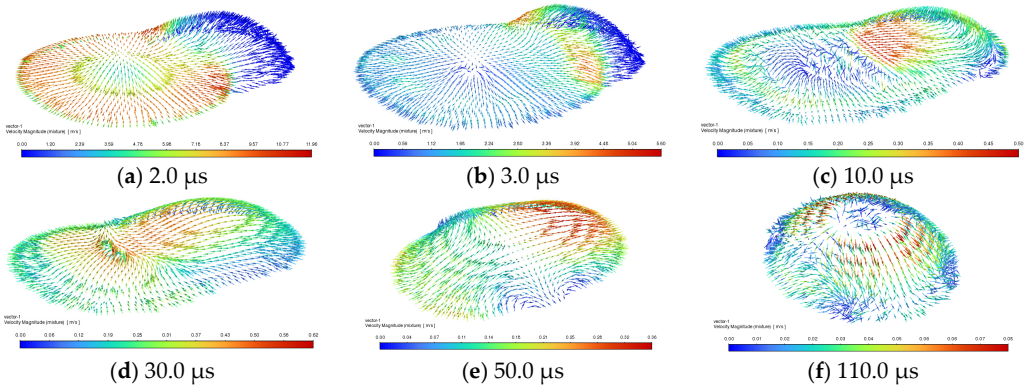
significantly, with a maximum of 0.5 m/s. Notably, the flow at the contact interface reverses direction, driving the droplet morphology to transition from separated to continuous.



(**a**) 2.0 μs (**b**) 3.0 μs (**c**) 10.0 μs

(**d**) 30.0 μs (**e**) 50.0 μs (**f**) 110.0 μs

Figure 10. Droplet interaction during impact at a spacing of 36 μm. (**a**) 2.0 μs; (**b**) 3.0 μs; (**c**) 10.0 μs; (**d**) 30.0 μs; (**e**) 50.0 μs; (**f**) 110.0 μs.



(**a**) 2.0 μs (**b**) 3.0 μs (**c**) 10.0 μs

(**d**) 30.0 μs (**e**) 50.0 μs (**f**) 110.0 μs

Figure 11. Distribution of droplet velocity vectors. (**a**) 2.0 μs; (**b**) 3.0 μs; (**c**) 10.0 μs; (**d**) 30.0 μs; (**e**) 50.0 μs; (**f**) 110.0 μs.

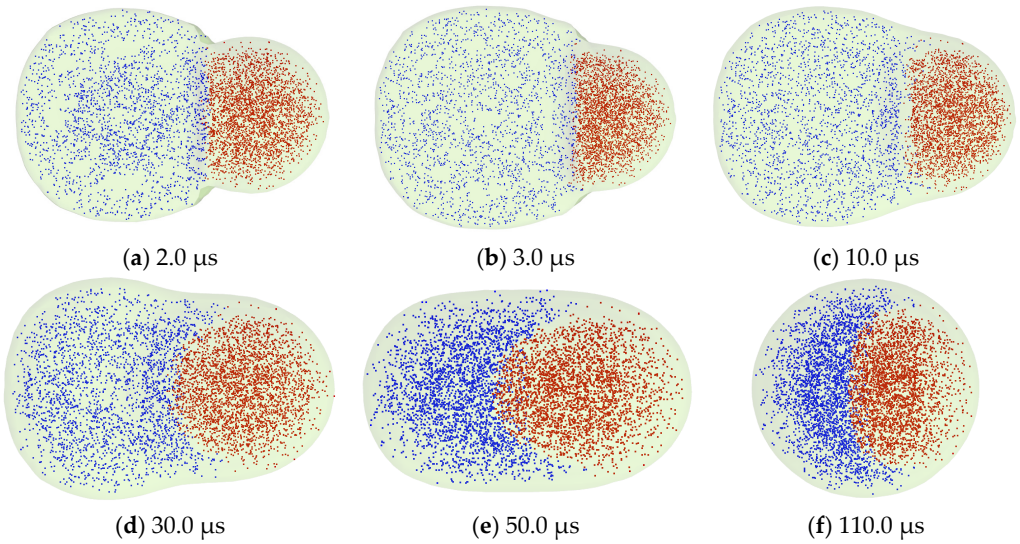
As coalescence proceeds, surface tension-driven contraction becomes dominant, redirecting the flow pattern to centripetal convection from the periphery toward the center. This inward flow progressively decreases in magnitude and becomes more uniformly distributed. Eventually, the internal motion stagnates as the droplet morphology stabilizes.

The distribution of diamond particles within the droplets was analyzed to trace material transport during coalescence, as shown in Figure 12, which corresponds to the time points in Figure 10. Red particles denote those within the initially deposited droplet, while blue particles represent those introduced by the later-falling droplet.

In the initial stage, as the later-falling droplet spreads upon impact, the blue particles are widely dispersed under inertial forces, moving toward the red particle region without intermixing; the interface between the two particle populations remains distinct. As coalescence proceeds, convection within the merging droplet drives red particles toward the blue region. Upon completion of coalescence and subsequent contraction to a steady state, the particle distribution stabilizes, revealing a characteristic crescent-shaped interface between the red and blue populations.

This morphology originates from the fusion dynamics: the spreading of the later-falling droplet exerts a confining effect on the already-stabilized droplet, encapsulating

its particles and resulting in the observed crescent-shaped boundary, with blue particles tending to envelop red particles.



(**a**) 2.0 μs (**b**) 3.0 μs (**c**) 10.0 μs

(**d**) 30.0 μs (**e**) 50.0 μs (**f**) 110.0 μs

Figure 12. Distribution of diamond powder within the droplet. (**a**) 2.0 μs; (**b**) 3.0 μs; (**c**) 10.0 μs; (**d**) 30.0 μs; (**e**) 50.0 μs; (**f**) 110.0 μs.

The elucidation of the low-speed deposition mechanism bridges a critical experimental knowledge gap and establishes a controllable parameter framework for coating fabrication on functional micro-milling cutter surfaces—including cutting edges and chip-clearance grooves. Insights into droplet dynamics—specifically their motion and diffusion behavior at the critical minimum deposition velocity—enable rational process integration of key parameters, such as nozzle orifice diameter, carrier gas flow rate, and droplet spacing. This optimization enhances both coating uniformity and geometric fidelity across complex micro-scale topographies, while mitigating undesirable phenomena including droplet splashing and overspray. Consequently, scalable, industrially viable fabrication of wear- and corrosion-resistant coatings on micro-milling cutters is now technically feasible.

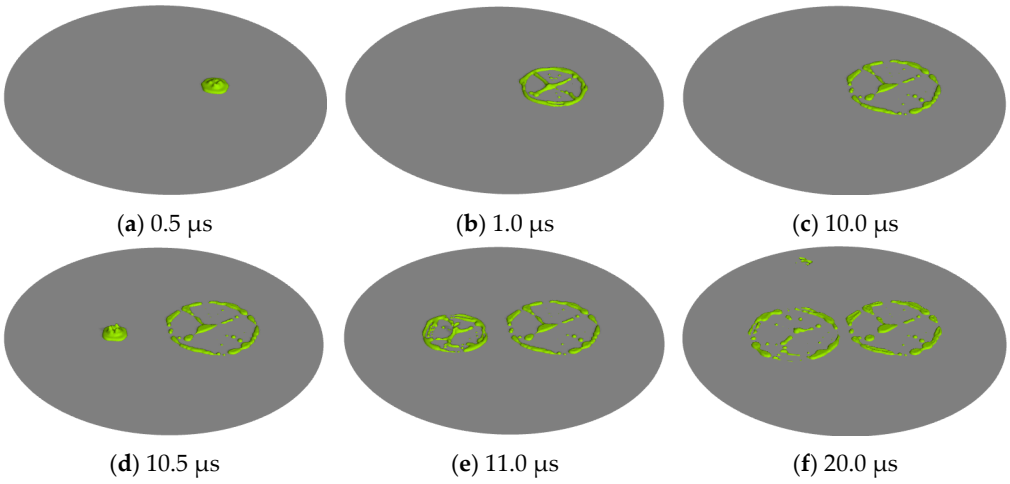
4. High-Speed Jet Printing Results and Discussion

Building on the analysis of droplet deposition behavior and evolution mechanisms at low jet velocities, this section presents a numerical investigation of ink droplet dynamics under high-speed injection conditions. The objective is to elucidate the role of injection flow rate in governing the uniformity of printed lines.

The simulation domain consists of a cylindrical region 110 μm in height and 480 μm in diameter. A main airflow rate of 65 mL/min was adopted, yielding a calculated droplet velocity of 137.06 m/s. Simulations were performed with a fixed printing line gap of 150 μm.

4.1. Analysis of Simulation Results

Figure 13 presents the simulated droplet deposition process under high-speed airflow conditions. Propelled by the high-velocity gas stream, the droplets acquire substantial kinetic energy, impacting the substrate and spreading into a dispersed circular pattern. Compared to the low-speed condition, droplet uniformity is reduced; however, the deposition behavior under high-speed conditions exhibits a distinct efficiency advantage. Stabilization is achieved at 20.0 μs under high-speed flow, representing a significant reduction in process cycle time relative to the low-speed case.



(**a**) 0.5 μs (**b**) 1.0 μs (**c**) 10.0 μs

(**d**) 10.5 μs (**e**) 11.0 μs (**f**) 20.0 μs

Figure 13. Simulated droplet deposition at a main airflow rate of 65 mL/min. (**a**) 0.5 μs; (**b**) 1.0 μs; (**c**) 10.0 μs; (**d**) 10.5 μs; (**e**) 11.0 μs; (**f**) 20.0 μs.

To quantify the spreading diameters of the two droplets at t = 20.0 μs, the liquid phase volume fraction along the bottom surface was analyzed. A Solution XY Plot was generated with the X-axis representing the lateral position along the substrate (−240 to 240 μm) and the Y-axis representing the liquid volume fraction (0 to 1), as shown in Figure 14.

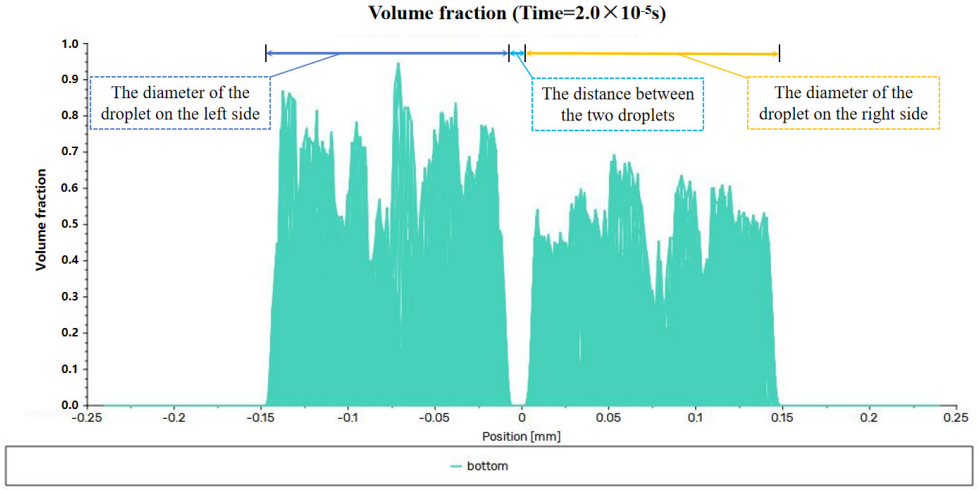


Figure 14. Solution XY Plot.

The results revealed that the liquid phase was distributed over two distinct intervals: from −146.22 to −7.31 μm on the left and from 3.60 to 147.09 μm on the right. From these intervals, the spreading diameters of the two droplets were calculated to be 138.91 μm and 143.49 μm, respectively. Compared to the low-speed condition, both droplets exhibited larger spreading diameters under high-speed injection. When the distance between the two droplets is 141.20 μm, the droplets can achieve the maximum spreading efficiency.

4.2. Experimental Verification

To validate the simulation results, a double-line printing experiment was conducted on a tungsten carbide substrate measuring 10 mm × 10 mm × 0.3 mm. The printing head was positioned 2 mm above the substrate, with a main airflow rate of 65 mL/min and a main-to-sheath airflow ratio of 1:2. The line gap in the experiment corresponded to the droplet spacing parameter in the simulations. Seven gap values were tested: 130, 140, 150, 180, 200, 220 and 250 μm. The morphology and uniformity of

the printed lines were examined using FEI Quanta 250 FEG scanning electron microscopy (FEI Company, Hillsboro, OR, USA). The relevant processing parameters and experimental conditions are summarized in Table 3. Table 4 presents the composition parameters of the ink.

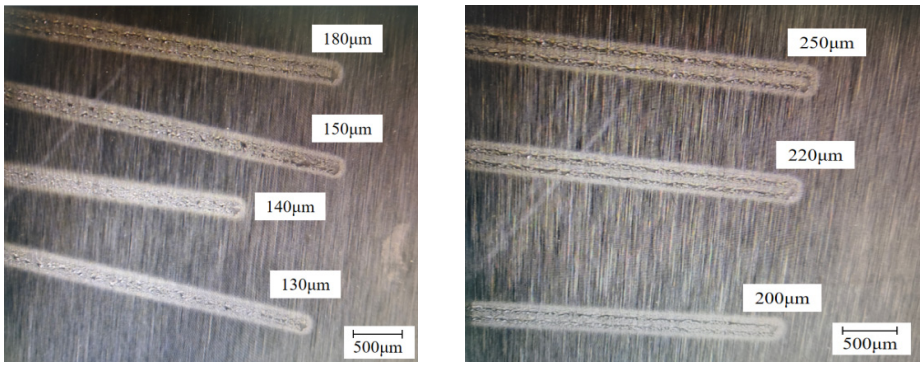
Table 3. Test parameters.

Project	Substrate Material	Distance Between the Print Head and the Substrate	Main Airflow Rate	Ratio of the Main Airflow to the Constrained Airflow
Parameters	Tungsten carbide	2 mm	65 mL/min	1:2

Table 4. Ink composition parameters.

Material	Volume (mL)
H_2O	25
SiO_2	0.1
EtOH (95 vol.%)	4
Sodium Dodecyl Sulfate	0.15
Polyethylene Glycol 400	3.8
Polycrystalline Diamond	1
Acetone	2
Adhesive	0.1

Figure 15 presents low-power microscope images of the printed lines from the validation experiments. The values displayed in white rectangles indicate the gap size for that line. Analysis of the seven test configurations reveals a clear threshold behavior. For line gaps $\geq$ 150 µm, the boundaries between adjacent lines remain distinctly separable. In contrast, for gaps $\leq$ 140 µm, the line boundaries become increasingly blurred, exhibiting a pronounced tendency toward inter-line merging.



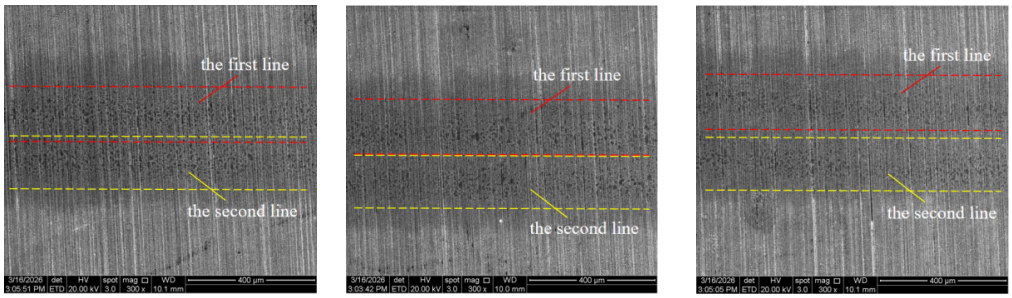
(**a**) (**b**)

Figure 15. Low-power microscope image of the printed lines. (**a**) 130–180 µm; (**b**) 200–250 µm.

High-magnification observations were performed using scanning electron microscopy (SEM) on three representative samples with line gaps of 130, 140, and 150 µm, as shown in Figure 16. Due to the inherent irregularities of the printed line edges—which exhibit significant undulations rather than ideally smooth contours—the maximum line width was adopted as the characteristic metric for statistical analysis.

The SEM images reveal distinct behaviors across the three gap settings. At a gap of 150 µm, the adjacent lines remain clearly separated with well-defined boundaries. At 130 µm, local overlapping between lines is observed. Notably, at 140 µm, the printed

lines exhibit optimal spreading efficiency, with adjacent lines achieving ideal coalescence without significant overlap.



(**a**) (**b**) (**c**)

Figure 16. Observation under scanning electron microscope. (**a**) 130 μm; (**b**) 140 μm; (**c**) 150 μm.

Comparison of this experimentally determined optimal spacing (140 μm) with the simulation prediction (141.20 μm) yields a relative deviation of only +1.20 μm. This agreement confirms that the established simulation model accurately captures droplet spreading behavior, thereby validating its rationality and the reliability of the computational results.

This study provides important theoretical support for the industrial application of aerosol jet printing to prepare diamond coatings for micro-milling tools. The established simulation model can accurately predict the coupling effect of droplet spacing and jet speed on the deposition morphology and line uniformity. Regarding the balance issue between deposition efficiency and coating uniformity that is commonly concerned in industrial production, the research results can provide direct reference for process parameter optimization and engineering solution formulation.

5. Conclusions

The simulation results of low-speed jetting reveal the dynamic evolution law of droplet deposition during aerosol jet printing. Under low-speed jetting conditions, after the droplets impact the substrate surface, they exhibit an evolution characteristic of rapid attenuation, brief stability, and slow rebound in the thickness direction, and in the diameter direction, they undergo rapid spreading and slow contraction stages, ultimately stabilizing as a spherical cap shape. When the spacing between adjacent printed lines is less than 42.15 μm, the droplets can achieve effective fusion, forming continuous lines without gaps. The above research results under low-speed conditions can provide an important reference basis for the mechanism analysis and result comparison of high-speed jetting processes.

Under high-speed jetting conditions, the liquid droplets exhibit a circular spreading dispersion characteristic. Relative to low-speed jetting, the resulting liquid film exhibits reduced uniformity but an expanded coverage area. Moreover, under high-speed conditions, the system achieves steady-state droplet deposition more rapidly, thereby enhancing overall deposition efficiency.

The developed simulation model demonstrates high accuracy in predicting droplet deposition behavior during aerosol jet printing, thereby offering robust theoretical guidance for experimental parameter selection for the preparation of high-quality coatings for milling tools and formation outcome prediction. Quantitative validation reveals that, under low-speed jetting conditions (main airflow velocity = 10 mL/min), the relative error between the simulated steady-state diameter of a single droplet and the corresponding theoretical value is +3.9%; under high-speed jetting conditions (main airflow velocity = 65 mL/min), the relative error in predicted droplet spacing is +0.85%. Overall, the absolute simulation error remains within ±10%. Excellent agreement between simulation and experimental results confirms the model's reliability, enabling deeper mechanistic insight into aerosol jet printing

physics and supporting data-informed optimization of the formation quality of the milling cutter coating lines. These findings provide important theoretical support for the industrial-scale fabrication of diamond coatings on micro-milling cutters via aerosol jet printing. For the industrially critical trade-off between deposition efficiency and coating uniformity, the results offer a valuable reference for process design and parameter optimization.

Future research will extend the present work by systematically investigating the coupled thermal and mass transfer mechanisms involved in the subsequent stages of diamond coating fabrication, including solvent removal, binder burnout, and sintering, as well as their influences on coating microstructure evolution, adhesion strength, wear resistance, and cutting performance. Furthermore, establishing the quantitative correlations among printing parameters, coating evolution behavior, and final machining performance will provide deeper insights into process optimization and contribute to the development of high-performance diamond-coated milling tools fabricated via aerosol jet printing.

Author Contributions: Conceptualization, H.C. and Q.Y.; methodology, Q.Y.; software, H.C.; validation, X.X.; formal analysis, M.U.; writing—original draft preparation, H.C.; writing—review and editing, Q.Y. All authors have read and agreed to the published version of the manuscript.

Funding: This research was funded by Henan Province's Science and Technology Research Project (Grant No.: 262102220069), High-talented Foreign Expert Cooperation Project of Zhengzhou Science and Technology Bureau (Grant No.: ZZGDHZ2025007), and Basic Research and Applied Basic Research Project, Zhengzhou Municipal Science and Technology Bureau (Grant No.: ZZSZX202429).

Institutional Review Board Statement: Not applicable.

Informed Consent Statement: Not applicable.

Data Availability Statement: The original contributions presented in this study are included in the article. Further inquiries can be directed to the corresponding author.

Conflicts of Interest: The authors declare no conflicts of interest.

Abbreviations

The following abbreviations are used in this manuscript:

AJP	Aerosol Jet Printing
CFD	Computational Fluid Dynamics
VOF	Volume of Fluid
DPM	Discrete Phase Model
CVD	Chemical Vapor Deposition
PVD	Physical Vapor Deposition

References

1. Han, J.; Ma, R.; Hao, X.; Kong, L.; Chen, N.; Li, L.; He, N. Experimental Research on Deep-And-Narrow Micromilled Grooves Using a Self-Fabricated PCD Micro-Cutter. *Micromachines* **2021**, *12*, 1170. [CrossRef] [PubMed]
2. Silva, E.L.; Pratas, S.; Neto, M.A.; Fernandes, C.M.; Figueiredo, D.; Silva, R.F. Multilayer Diamond Coatings Applied to Micro-End-Milling of Cemented Carbide. *Materials* **2021**, *14*, 3333. [CrossRef] [PubMed]
3. Heaney, P.J.; Sumant, A.V.; Torres, C.D.; Carpick, R.W.; Pfefferkorn, F.E. Diamond coatings for micro end mills: Enabling the dry machining of aluminum at the micro-scale. *Diam. Relat. Mater.* **2008**, *17*, 223–233. [CrossRef]
4. Guyll, B.I.; Petersen, L.D.; Pint, C.L.; Secor, E.B. Enhanced Resolution, Throughput, and Stability of Aerosol Jet Printing via In Line Heating. *Adv. Funct. Mater.* **2024**, *34*, 2316426. [CrossRef]
5. Ali, M.A.; Hu, C.; Jahan, S.; Yuan, B.; Saleh, M.S.; Ju, E.; Gao, S.J.; Panat, R. Sensing of COVID-19 Antibodies in Seconds via Aerosol Jet Nanoprinted Reduced-Graphene-Oxide-Coated 3D Electrodes. *Adv. Mater.* **2021**, *33*, 2006647. [CrossRef] [PubMed]
6. Ramesh, S.; Mahajan, C.; Gerdes, S.; Gaikwad, A.; Rao, P.; Cormier, D.R.; Rivero, I.V. Numerical and experimental investigation of aerosol jet printing. *Addit. Manuf.* **2022**, *59*, 103090. [CrossRef]

7. Bozkurt, Y.; Karayel, E. 3D printing technology; methods, biomedical applications, future opportunities and trends. *J. Mater. Res. Technol.* **2021**, *14*, 1430–1450. [CrossRef]
8. Gebler, M.; Schoot Uiterkamp, A.J.M.; Visser, C. A global sustainability perspective on 3D printing technologies. *Energy Policy* **2014**, *74*, 158–167. [CrossRef]
9. Radenkovic, D.; Solouk, A.; Seifalian, A. Personalized development of human organs using 3D printing technology. *Med. Hypotheses* **2016**, *87*, 30–33. [CrossRef] [PubMed]
10. Long, Y.; Pan, J.; Zhang, Q.; Hao, Y. 3D printing technology and its impact on Chinese manufacturing. *Int. J. Prod. Res.* **2016**, *55*, 1488–1497. [CrossRef]
11. Wilkinson, N.J.; Smith, M.A.A.; Kay, R.W.; Harris, R.A. A review of aerosol jet printing—A non-traditional hybrid process for micro-manufacturing. *Int. J. Adv. Manuf. Technol.* **2019**, *105*, 4599–4619. [CrossRef]
12. Jin, Y.; Yi, H.; Cao, H.; Dong, X. Full-process aerosol jet printing modelling: Achieving high-fidelity simulation via coupling jetting and deposition. *Virtual Phys. Prototyp.* **2025**, *20*, e2516665. [CrossRef]
13. Liu, Z.; Liu, Y.; He, L.; Cui, L.; Liang, N.; Choi, J.P.; Zhang, H. A Comprehensive Investigation of Process Parameters and Material Properties Effects on Printed Line Quality of Aerosol Jet Printing Based on Coupled Three-dimensional Numerical Models. *Int. J. Precis. Eng. Manuf. Technol.* **2024**, *11*, 727–742. [CrossRef]
14. Elkaseer, A.; Schneider, S.; Scholz, S. Geometrical-based Simulation of Drop-on-Demand 3D Inkjet Printing. In Proceedings of the World Congress on Micro and Nano Manufacturing, Mumbai, India, 20–23 September 2021.
15. Shah, R.; Mohan, R.V. Computational Modeling of Droplet-Based Printing Using Multiphase Volume of Fluid (VOF) Method: Prediction of Flow, Spread Behavior, and Printability. *Fluids* **2025**, *10*, 123. [CrossRef]
16. Ari, A.; Fink, J.B. Quantifying Delivered Dose with Jet and Mesh Nebulizers during Spontaneous Breathing, Noninvasive Ventilation, and Mechanical Ventilation in a Simulated Pediatric Lung Model with Exhaled Humidity. *Pharmaceutics* **2021**, *13*, 1179. [CrossRef] [PubMed]
17. Hu, M.; Zhou, J.; Li, Y.; Zhuo, X.; Jing, D. Effects of the surface wettability of nanoparticles on the impact dynamics of droplets. *Chem. Eng. Sci.* **2021**, *246*, 116977. [CrossRef]
18. Yi, H.; Li, J.; Wang, Z.; Cao, H.; Liu, M. Elimination of gas entrapment in droplet-based 3D printing by induced electric-field. *Int. J. Mech. Sci.* **2024**, *266*, 108974. [CrossRef]
19. Yi, H.; Wang, Z.; Li, J.; Luo, J.; Cao, H.; Qi, L. Gas entrapment and pore formation in metal droplet-based 3D printing. *Int. J. Mech. Sci.* **2023**, *264*, 108810. [CrossRef]
20. Pasandideh-Fard, M.; Qiao, Y.M.; Chandra, S.; Mostaghimi, J. Capillary effects during droplet impact on a solid surface. *Phys. Fluids* **1996**, *8*, 650–659. [CrossRef]
21. Feng, J.Q.; Optomec, I. A Computational Study of High-Speed Microdroplet Impact onto a Smooth Solid Surface. *J. Appl. Fluid Mech.* **2017**, *10*, 243–256. [CrossRef]
22. Adeniyi, A.A.; Morvan, H.P.; Simmons, K.A. A coupled Euler-Lagrange CFD modelling of droplets-to-film. *Aeronaut. J.* **2017**, *121*, 1897–1918. [CrossRef]
23. Yokoi, K.; Vadillo, D.; Hinch, J.; Hutchings, I. Numerical studies of the influence of the dynamic contact angle on a droplet impacting on a dry surface. *Phys. Fluids* **2009**, *21*, 072102. [CrossRef]
24. Wang, L.-S.; Krull, B.; Lucas, D.; Meller, R.; Schlegel, F.; Tekavčič, M.; Xu, J.-Y. Simulation of droplet entrainment in annular flow with a morphology adaptive multifield two-fluid model. *Phys. Fluids* **2023**, *35*, 103312. [CrossRef]
25. Ramesh, S.; Xu, Z.; Rivero, I.V.; Cormier, D.R. Computational fluid dynamics and experimental validation of aerosol jet printing with multi-stage flow focusing lenses. *J. Manuf. Process.* **2023**, *95*, 312–329. [CrossRef]
26. Yao, L.; Xiao, Z.; Liu, J.; Zhang, Q.; Wang, M. An optimized CFD-DEM method for fluid-particle coupling dynamics analysis. *Int. J. Mech. Sci.* **2020**, *174*, 105503. [CrossRef]
27. Hoey, J.M.; Lutfurakhmanov, A.; Schulz, D.L.; Akhatov, I.S. A Review on Aerosol-Based Direct-Write and Its Applications for Microelectronics. *J. Nanotechnol.* **2012**, *2012*, 1–22. [CrossRef]
28. Michaelides, E.E.; Sommerfeld, M.; van Wachem, B. *Multiphase Flows with Droplets and Particles*, 3rd ed.; Taylor & Francis: London, UK, 2022; pp. 1–478.
29. Qenawy, M.; Chen, Y.; Wang, J.; Tian, J.; Li, B.; Chen, B. Transient behavior of liquid film deposition and surface heat transfer upon cryogen-spray cooling coupled with cold air jet. *Int. J. Heat Mass Transf.* **2024**, *223*, 125224. [CrossRef]
30. Hutchings, I.M.; Martin, G.D.; Hoath, S.D. *Fundamentals of Inkjet Printing: The Science of Inkjet and Droplets*; Wiley-VCH Verlag GmbH & Co. KGaA: Weinheim, Germany, 2015; pp. 339–364.
31. Stringer, J.; Derby, B. Formation and Stability of Lines Produced by Inkjet Printing. *Langmuir* **2010**, *26*, 10365–10372. [CrossRef] [PubMed]

32. Derby, B. Inkjet Printing of Functional and Structural Materials: Fluid Property Requirements, Feature Stability, and Resolution. *Annu. Rev. Mater. Res.* **2010**, *40*, 395–414. [CrossRef]
33. Gururaja, S.; Singh, K.K. Surface Form Error Prediction in High-Speed Micromilling of Thin-Walled TC4 Alloys: A Stacking-Based Ensemble Approach. *J. Micro Nano Sci. Eng.* **2026**, *14*, 011003. [CrossRef]

Disclaimer/Publisher's Note: The statements, opinions and data contained in all publications are solely those of the individual author(s) and contributor(s) and not of MDPI and/or the editor(s). MDPI and/or the editor(s) disclaim responsibility for any injury to people or property resulting from any ideas, methods, instructions or products referred to in the content.